Isotope Exchange Raman Spectroscopy (IERS): A Novel Technique to Probe Physicochemical Processes In Situ

Alexander Stangl, Dolors Pla, Caroline Pirovano, Odette Chaix-pluchery, Federico Baiutti, Francesco Chiabrera, Albert Tarancón, Carmen Jiménez, Michel Mermoux, Mónica Burriel

ADVANCED MATERIALS
www.advmat.de

Isotope Exchange Raman Spectroscopy (IERS): A Novel Technique to Probe Physicochemical Processes In Situ

Alexander Stangl, Dolors Pla, Caroline Pirovano, Odette Chaix-Pluchery, Federico Baiutti, Francesco Chiabrera, Albert Tarancón, Carmen Jiménez, Michel Mermoux, and Mónica Burriel**

A novel in situ methodology for the direct study of mass-transport properties in oxides with spatial and unprecedented time resolution, based on Raman spectroscopy coupled to isothermal isotope exchanges, is developed. Changes in the isotope concentration, resulting in a Raman frequency shift, can be followed in real time, which is not accessible by conventional methods, enabling complementary insights for the study of ion-transport properties of electrode and electrolyte materials for advanced solid-state electrochemical devices. The proof of concept and strengths of isotope exchange Raman spectroscopy (IERS) is demonstrated by studying the oxygen isotope back-exchange in gadolinium-doped ceria (CGO) thin films. Resulting oxygen self-diffusion and surface exchange coefficients are compared to conventional time-of-flight secondary-ion mass spectrometry (ToF-SIMS) characterization and literature values, showing good agreement, while at the same time providing additional insight, challenging established assumptions. IERS captivates through its rapidity, simple setup, non-destructive nature, cost effectiveness, and versatile fields of application and thus can readily be integrated as new standard tool for in situ and operando characterization in many laboratories worldwide. The applicability of this method is expected to consolidate the understanding of elementary physicochemical processes and impact various emerging fields including solid oxide cells, battery research, and beyond.

1. Introduction

Many types of advanced solid-state electrochemical devices, spanning over a large range of applications from energy conversion, transport, and storage, environmental gas sensing to neuromorphic computing, are built upon versatile ionic and/or electronic conducting materials, where ion kinetics are key to the functional properties. Oxides are at the center of this emerging materials class.[1] Accelerating the development of tuned metal oxides is therefore an integral part toward high performance and miniaturized electrochemical systems. This strategy requires innovative approaches to materials synthesis[2] and nano-engineering,[3] as well as a constantly expanding toolbox for deeper fundamental understandings. Time and cost intensive techniques based on large scale facilities or lab based cutting edge experimental setups (e.g., synchrotron, in situ transmission electron microscopy (TEM),[4] near-ambient-pressure Xray photoelectron spectroscopy (NAP-XPS), etc.[5]) contribute with outstanding insights into highly relevant physicochemical

A. Stangl, D. Pla, O. Chaix-Pluchery, C. Jiménez, M. Burriel
Univ. Grenoble Alpes
CNRS
Grenoble-INP, LMGP, Grenoble 38000, France
E-mail: alexander.stangl@grenoble-inp.fr;
monica.burriel@grenoble-inp.fr

C. Pirovano
Univ. Lille, CNRS
Centrale Lille
Univ. Artois
UMR 8181 – UCCS – Unité de Catalyse et Chimie du Solide, Lille F-59000, France

The ORCID identification number(s) for the author(s) of this article can be found under https://doi.org/10.1002/adma.202303259

DOI: 10.1002/adma.202303259

F. Baiutti, F. Chiabrera, A. Tarancón
Catalonia Institute for Energy Research (IREC)
Barcelona 08930, Spain

F. Baiutti
Departement of Materials Chemistry
National Institute of Chemistry
Hajdrihova 19, Ljubljana SI-1000, Slovenia

A. Tarancón
ICREA
23 Passeig Lluis Companys, Barcelona 08010, Spain

M. Mermoux
Univ. Grenoble Alpes
Univ. Savoie Mont Blanc
CNRS, Grenoble INP, LEPMI, Grenoble 38000, France

processes with remarkable spatial and temporal resolution. However, the widespread availability of advanced characterization techniques, especially focusing on in situ and operando characterization,[6–8] is essential for the efficient and timely material studies with high-throughput capabilities. Traditionally, oxygen transport properties are addressed by three approaches: electrochemical impedance spectroscopy (EIS), electrical conductivity relaxation (ECR), and isotope exchange depth profiling coupled to secondary-ion mass spectrometry (IEDP-SIMS). Each one is characterized by certain benefits and limitations in terms of applicability, costs, information depth, and preservation of sample integrity. Here, we aim to expand the scientific toolkit by introducing a novel, readily accessible in situ methodology based on the coupling of isotopic exchange with micro Raman spectroscopy for the characterization of mass-transport kinetics in real time, without the need of expensive and/or time-consuming techniques.

Raman spectroscopy is known as a powerful and efficient, yet standard tool for assessing the microstructure and defect landscape of various types of materials including metal oxides. In particular, it has a long lasting and successful history for in situ characterization of catalyst materials[9–11] and lithium intercalation in battery electrodes[12–15] using visible light. Raman spectroscopy is generally considered a vibrational spectroscopy technique and, as such, sensitive to the mass of the atoms constituting a crystal. The isotopic substitution thus provides a mass contrast, which can be utilized for the assignment of vibrational modes,[16] the study of isotopic fractions,[17] or irradiation effects[18] and to investigate bevelled surfaces for isotopic depth profiling.[19,20] However, there are only a few works that combine in situ Raman spectroscopy with $^{18}O/^{16}O$ isotopic substitution,[21,22] focussing on surface structures,[23–25] rather than exchange kinetics. Oxygen self-diffusion in Y_2O_3–ZrO_2 bulk has only been addressed indirectly by Raman spectroscopy by following the amount of ^{18}O tracer atoms in the ambient gas.[26] Finally, and only very recently, in situ Raman measurements have been employed to extract kinetic coefficients via hydrogen/deuterium exchange by tracking the fraction of Raman band intensities.[27–29]

In this study, we take advantage of the mass sensitivity of Raman spectroscopy and demonstrate the possibility to follow continuous temporal changes in the vibrational frequency spectra as a function of the isotopic concentration of oxygen by in situ Raman spectroscopy for the characterization of tracer exchange and diffusion properties and thus, make oxygen movement inside a material visible. To the best of our knowledge, this is the first time that oxygen tracer exchange processes can be directly followed in real time by any means. This methodology can be readily expanded to other fields of application, including e.g., the study of isotopically labeled Li in Li-ion batteries and O in new O-ion batteries,[30] heralding a new era of tracer-based experiments.

In the following section, the fundamentals of the isotope effect on the Raman spectra are briefly introduced and the novel in situ isotope exchange Raman spectroscopy (IERS) methodology is presented, including a discussion on requirements, advantages, and limitations. Finally, surface exchange coefficients with corresponding activation energies and in-plane diffusion coefficients for $Ce_{0.8}Gd_{0.2}O_{2-\delta}$ thin films are reported for in situ measurements and compared to values obtained by the conventional ToF-SIMS approach and literature.

2. Methods

2.1. Isotope Effect in Raman Spectroscopy

As vibrational spectroscopy technique Raman spectroscopy is sensitive to the mass of the atoms constituting a molecule or a crystal. Within the framework of the harmonic approximation, the wavenumber, ω, of a specific vibrational mode is proportional to:

$$\omega \propto \sqrt{\frac{k}{\mu}} \tag{1}$$

where k is a spring constant and μ the reduced mass. Here, the effective reduced mass provides chemical and/or isotopic information. The virtual crystal approximation (VCA) is usually introduced for a crystal containing several isotopes in order to recover the translational invariance lifted by the isotopic disorder, meaning that masses of these isotopes are simply replaced by their average weighted relative abundances, $\bar{m}$.[31,32] This approximation allows to understand the one mode behavior observed for monoatomic crystals as well as for crystals with different elements in the primitive cell, i.e., the isotopic mass disorder is only a weak perturbation of the crystal properties.

While IERS can be applied using different isotopic tracer elements, including ^6Li and ^{18}O, we will restrict ourselves in the following to the latter. The analysis for O-dominated or purely oxygen related vibrational modes is straightforward. The mass of the virtual crystal atoms is given by:

$$\bar{m} = {}^{18}C \cdot \bar{m}_{^{18}O} + (1 - {}^{18}C)\bar{m}_{^{16}O} \tag{2}$$

with the atomic weights $m_{^{18}O} = 17.999$ u and $m_{^{16}O} = 15.995$ u of ^{18}O and ^{16}O, respectively and the ^{18}O isotopic fraction:

$${}^{18}C = \frac{[^{18}O]}{[^{18}O] + [^{16}O]} \tag{3}$$

Since the force constants, in the harmonic approximation, are constant, the relative shift due to isotopic substitution, can be estimated within the VCA model using Equation 1:

$$\frac{\omega({}^{18}C)}{\omega_{\text{ref}}} = \sqrt{\frac{\mu_{\text{ref}}}{\mu({}^{18}C)}} = \sqrt{\frac{\bar{m}_{\text{ref}}}{\bar{m}({}^{18}C)}} \tag{4}$$

and thus $\omega \propto {}^{18}C^{-1/2}$

2.2. In situ Isotope Exchange Raman Spectroscopy

IERS is based on the sensitivity of Raman spectroscopy to isotopic fractions. Upon thermal activation of oxygen isotopic exchange by heating a sample in a gas atmosphere of isotopic concentration different from the specimen, the Raman shift can be followed in situ with time and spatial resolution (see **Figure 1**). IERS can be applied to study the exchange (i.e., introducing ^{18}O into the sample) as well as the back-exchange

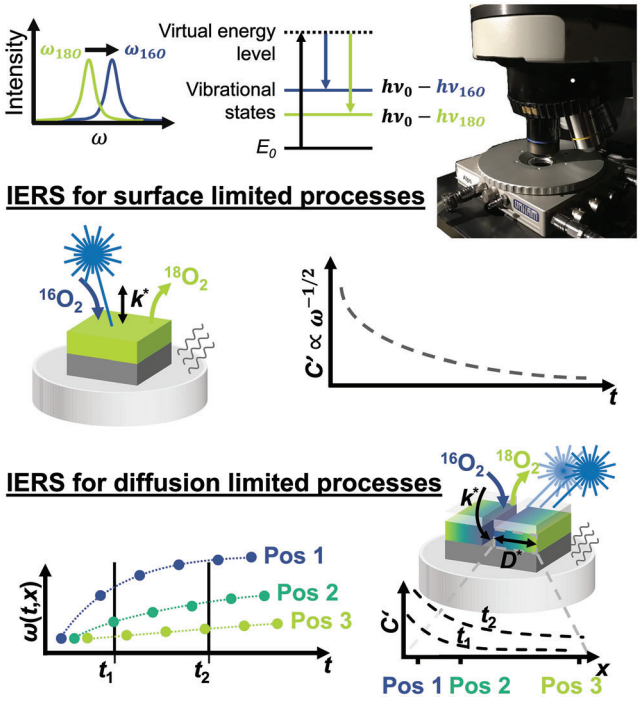

Figure 1. Schematic of novel IERS methodology to study surface and diffusion limited processes, based on isotopic Raman shifts.

(i.e., removing ^{18}O from the sample) as a function of temperature, pressure, humidity, gas constituents, etc. in a non-destructive manner. Studying the back-exchange, however, allows to drastically reduce the tracer gas consumption and enables the use of conventional temperature cells. To obtain meaningful transients, exchanges must be performed under isothermal conditions.

We developed two scenarios for the application of in situ IERS. The first one, for the direct characterization of the tracer surface exchange coefficient, k^*, is restricted to the study of surface limited reactions and thus to thin films and (nano-) powders. The measured transients can be related to a kinetic model, as outlined in the next section.

The second case expands the applicability of IERS to diffusion limited reactions (thin films and dense bulk materials) and gives access as well to the in-plane self diffusion coefficient, D^*. Therefore the sample is coated with a thin, Raman transparent and inert conformal capping layer to inhibit oxygen exchange at the surface. Next, a trench in the coating and film/bulk is opened, exposing the materials surface to the atmosphere and thus allowing oxygen exchange only along one well defined side.[33] This results in an in-plane isotopic concentration gradient during an isotope exchange, which can be followed by performing consecutive measurements at different distances from the open surface, as schematically shown in the lower panel of Figure 1. The diffusion profiles as a function of time, obtained by interpolation of the transients at each position, can be modeled by Fick's second law to retrieve tracer exchange and in-plane diffusion parameters. The time and spatial resolution of this technique enables an unparalleled analysis of tracer exchange and diffusion processes.

2.2.1. Theoretical Considerations on Mass-Transport Laws

The isotopic transitions can be analyzed within the framework of irreversible thermodynamics to obtain tracer surface oxygen exchange and bulk transport parameters, equivalent to the analysis performed in various time resolved relaxation techniques to obtain chemical transport coefficients, including electrical conductivity,[34] strain,[35] gravimetric,[36] and optical transmission[37] relaxation. Ideally, the driving force for IERS measurements is purely of thermodynamic origin, without any chemical gradients.

The oxygen tracer flux through the surface, J^*, can be developed as a function of the concentration difference across the interface:[38]

$$J^* = \sum_{i=0}^{\infty} k_i^* \left({}^{18}C_{\text{gas}} - {}^{18}C_{\text{surface}}(t)\right)^i \tag{5}$$

with the tracer concentration in the atmosphere, ${}^{18}C_{\text{gas}}$ and the outermost surface layer of the solid, ${}^{18}C_{\text{surface}}(t)$ and the tracer surface exchange coefficient, k_i^*. For simple homogenous kinetics and small deviations from equilibrium, its expansion is commonly cut after the linear term.[39]

Using Equation (5) in its linear form and a plane sheet geometry the solution to Fick's second diffusion law in the case of a single rate determining step (RDS) within the surface is given by:

$$C'(t) = \frac{{}^{18}C(t) - {}^{18}C_{\text{ini}}}{{}^{18}C_{\text{gas}} - {}^{18}C_{\text{ini}}} \propto \frac{\omega(t) - \omega_{\text{ini}}}{\omega_{\infty} - \omega_{\text{ini}}} \tag{6}$$

$$= \begin{cases} 1 - \exp^{-t/\tau} & \text{(6a)} \\ 1 - \sin^2 a \exp^{-t/\tau_\alpha} - \cos^2 a \exp^{-t/\tau_\beta} & \text{(6b)} \end{cases}$$

with the normalized isotopic fraction, C', the ^{18}O abundance within the sample at $t = 0$ and the gas phase, ${}^{18}C_{\text{ini}}$ and ${}^{18}C_{\text{gas}}$, respectively. The characteristic time constant, τ, in Equation 6a is linked to the rate-limiting step via $\tau = d_f/k^*$, with the film thickness, d_f. However, it is often found that a single exponential decay does not describe sufficiently well the experimental data, which is compensated by introducing a parallel contribution using two time constants, τ_α and τ_β, and a weighting factor, a, as given in Equation (6b). This is commonly explained by differences in exposed surface areas, such as grain and grain boundary or different terminations.[3,40–42] Additionally, we consider the case of a non-linear reaction rate by expanding Equation (5) to the second order. For a surface limited reaction the solution of Fick's law becomes:

$$C'(t) = 1 - \frac{\tau_2}{(\tau_1 + \tau_2)\exp[t/\tau_1] + \tau_1} \tag{7}$$

with $k_i^* = d_f/\tau_i$

2.2.2. Discussion on the Novel IERS Methodology

Before moving on to the results section, we would like to review the outlined IERS methodology and address several potential

issues, such as thermally induced stress, time resolution and laser light related effects. First, fast heating ramps are recommended to minimize isotopic exchange during the heating and to obtain the best time resolution. However, heating rates have to be defined within a material specific range to avoid the formation of cracks and thus damage of the oxide surface, as this could alter the observed isotope exchange rates, e.g., by increasing the exposed surface area, or the exposure of different surface terminations. For the accurate measurements the material under investigation must be able to withstand the thermally induced stress. However, IERS is also applicable to materials that cannot withstand fast ramps, at the expense of time resolution at the initial stage. In this case, the isotopic exchange during the heating ramp can be quantified using a thermal calibration at low temperatures, as discussed below. In general, slow heating/cooling rates can be used when measuring at either reduced temperatures or for materials with slower mass-transport properties.

Second, the spectrum acquisition time must be small compared to the time constant of the exchange process in order to provide sufficient time resolution while ensuring an adequate signal-to-noise ratio and avoiding an artificial line broadening. This requirement defines a material specific upper temperature limit for the applicability of IERS.

Third, laser induced heating and/or photoenhanced activity can potentially affect the thermally activated intrinsic exchange activity of the material. Photoenhanced activation of oxygen exchange is long known[43,44] and is understood via the formation of e'–$h^{\bullet}$ pairs across the bandgap (for $h\nu > E_{gap}$), which increases the electron concentration in the conduction band.[45,46] Provided that electrons are the rate determining species of oxygen incorporation, irradiation may enhance the surface exchange rates. Additionally, it was shown recently that ionic conductivity of CGO grain boundaries can be significantly improved upon illumination with above bandgap light.[47] Material dependent effects of laser light irradiation either due to direct laser heating or photoenhanced activity have to be excluded for accurate assessment of transport kinetics, as discussed below.

3. Results and Discussion

3.1. Structural and Chemical Characterization

Polycrystalline $Ce_{0.8}Gd_{0.2}O_{2-\delta}$ thin films were deposited by PLD on Pt/Si substrates (see experimental for more details). The film thicknesses of the studied samples were about 120 nm with a dense structure, nanometric grains (48 ± 23 nm) and low roughness (R_q = 1.6 nm). A summary of their main characteristics is shown in Figure S1 (Supporting Information).

Cerium oxide has the cubic fluorite structure (O_h^5 (Fm-3m) space group). This structure has six optical-phonon branches, which yield one infrared active phonon of T_{1u} symmetry and one Raman active phonon of T_{2g} symmetry at $k = O$. The infrared and Raman active modes involve the antisymmetric and symmetric stretching vibrations of the cation–oxygen O–Ce–O units, respectively. The Raman-active mode therefore only involves the motion of oxygen atoms. For undoped cerium oxide, this mode is observed at approximately 465 cm^{-1}.

The Raman spectrum of an as deposited CGO thin film with natural ^{18}O isotopic abundance (0.2%) is shown in Figure S1a (Supporting Information) (see also **Figure 2**b). While its main band still arises around 465 cm^{-1}, doping with trivalent rare earth cations, like Gd^{3+} creates a symmetry breaking in the lattice, resulting in a long tail evolving on the left shoulder of the band[48] and two additional features between 550 and 600 cm^{-1} in the Raman spectrum of CGO. These additional bands are disorder-induced modes related to oxygen vacancies created to maintain charge neutrality when Gd^{3+} ions are incorporated in Ce^{4+} sites, according to $2[Gd'_{Ce}]=[V_O^{\cdot\cdot}]$.[49] The contribution of the Si substrate is effectively blocked by the metallic Pt buffer layer. This buffer layer is not a requirement for IERS measurements, but allows for the case of CGO deposited on silicon substrate to improve the overall Raman signal quality. The T_{2g} mode position is obtained by line fitting, as exemplarily shown in Figure S2a (Supporting Information).

Subsequently, some of the CGO films were enriched in ^{18}O. The elemental and isotopic concentration as a function of film thickness was analyzed by ToF-SIMS for several samples at different stages of ^{18}O enrichment, as shown in Figure 2a for a CGO sample exchanged at 640 °C (0.5 h) and two samples partially ^{16}O back-exchanged at 400 °C (1 h and 20 h, respectively). For all studied films, the resulting ^{18}C curves are flat. The absence of a diffusion profile indicates that the oxygen exchange is limited by surface processes, while bulk diffusion is comparably fast. The depth profiles of selected secondary-ion species are shown in Figure S3 (Supporting Information) for a CGO sample after ^{18}O exchange at 640 °C.

The substitution of heavy oxygen into the crystal lattice effectively leads to a modification of the vibrational spectra and results in a red shift of the T_{2g} mode of about 20 cm^{-1}, i.e., 4.3%, between the ^{16}O reference and ^{18}O exchanged CGO sample, as shown in Figure 2b. The strong downshift of the defect-induced lines upon ^{18}O substitution confirms that these modes involve oxygen motion as well.

The dependence of the maximum position of the T_{2g} mode, ω_{max}, on the isotopic concentration is shown in Figure 2c, with the ^{18}O filling level measured by ToF-SIMS. The dashed line shows the best fit of experimental data using the VCA model, as given by Equation 4. The observed line shifts correspond to those expected, within the experimental accuracy. Thus, ^{18}C can be precisely assessed via Raman spectroscopy, see also Figure S4 (Supporting Information).

It is worthwhile to note that in off-resonant conditions (as is the case here) the penetration depth of the laser exceeds the film thickness. The isotopic concentration, obtained via the measured Raman shift, therefore corresponds to an average concentration across the film thickness. Any inhomogeneous ^{18}O concentration along the out of plane direction is expected to lead to a modification of the line shape of the T_{2g} mode, i.e., the peak width and profile. This is not observed in the present films and a homogenous oxygen concentration can be assumed, in agreement with flat SIMS depth profiles. Thus, the T_{2g} mode frequency is the only information needed to determine the ^{18}O content in the thin films.

Finally, the evolution of the Raman spectra with temperature is shown in Figure S5a (Supporting Information). The T_{2g} mode remains well defined at elevated temperatures, while

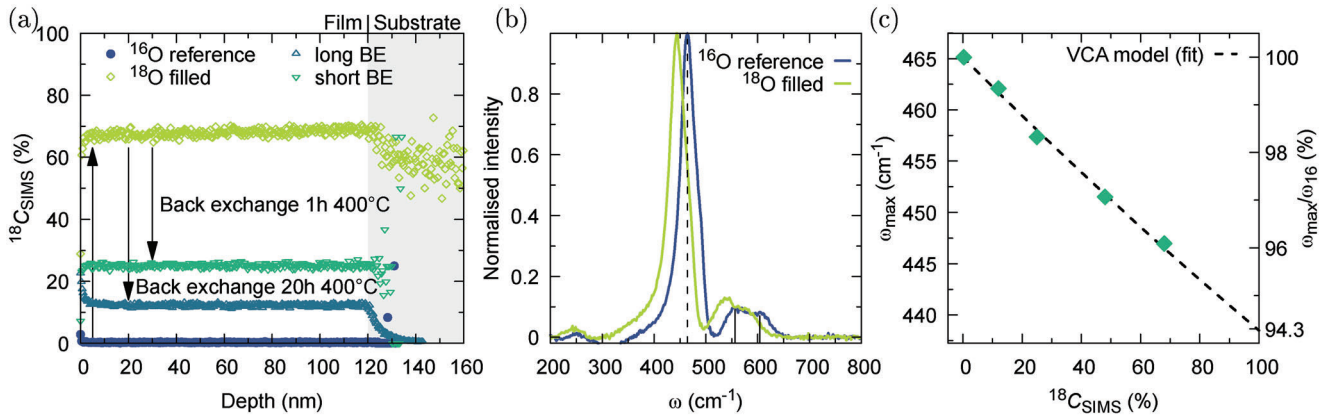

Figure 2. Isotopic Raman shift. a) ToF-SIMS ^{18}O depth profiles for ^{16}O annealed reference sample, ^{18}O exchanged film and two films back-exchanged at 400 °C for 1 and 20 h, respectively. b) ^{18}O-induced shift as observed by Raman spectroscopy. c) Correlation of Raman shift and the isotopic concentration. The dashed line is the fit of the data to the virtual crystal approximation (VCA).

thermal expansion of the lattice and anharmonic effects both induce a quite linear shift of its maximum position to lower wavenumbers, as depicted in Figure S5b (Supporting Information), accompanied by a broadening of the mode. The frequency of the T_{2g} mode of both, ^{16}O reference and ^{18}O enriched films exhibit a very similar temperature dependence, i.e., the isotopic shift, $\Delta\omega$, remains approximately constant with temperature. Combining Equation (4) with the linear temperature shift, hence allows to obtain in situ the ^{18}C concentration at elevated temperatures based on the measurement of Raman frequencies.

3.2. IERS for Surface Limited Thin Film Scenario

The strengths of IERS for the analysis of surface limited kinetics are demonstrated by the study of CGO thin films. The in situ isotopic shift of the Raman spectrum is shown in **Figure 3**a for a back-exchange experiment in dry air atmosphere at 400 °C. The

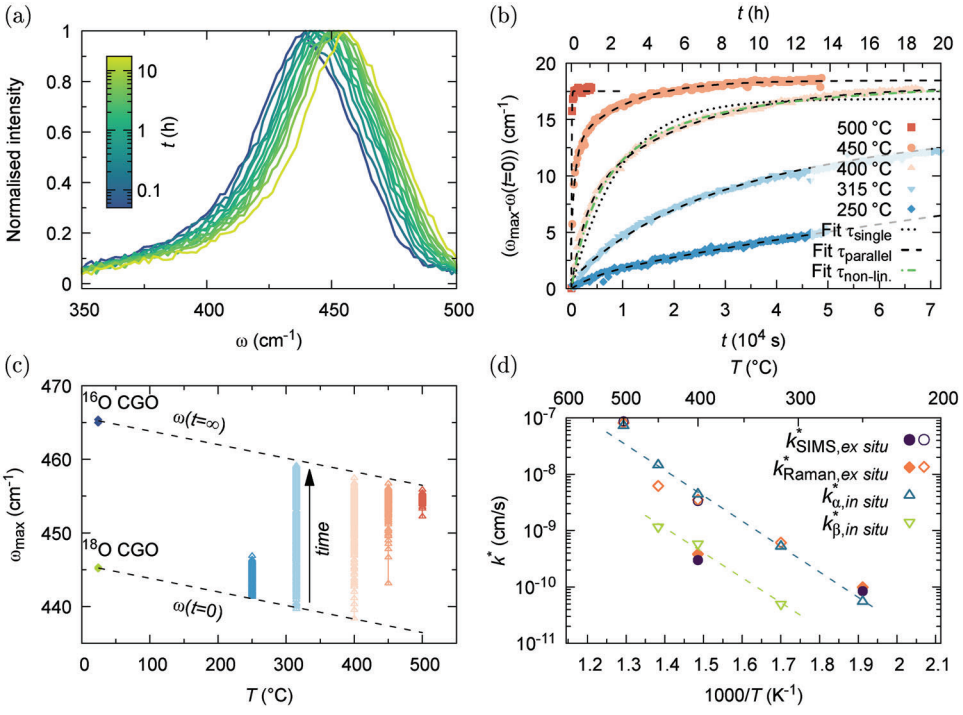

Figure 3. In situ isotopic exchange Raman spectroscopy. a) Raman spectrum of CGO as a function of time at 400 °C. b) In situ back-exchange transients at different temperatures in flowing dry air ($pO_2 = 0.21$ atm). Dotted, dashed, and dashed-dotted lines through the 400 °C data set correspond to single and double exponential fittings (τ_{single} and $\tau_{parallel}$) and the non-linear reaction rate model ($\tau_{non\text{-}lin.}$). c) Shift from initial ($\omega(t=0)$) ^{18}O to (expected) final ^{16}O state in a (ω_{max}–T) diagram. d) Arrhenius-type plot of the surface exchange coefficient, k^*, obtained by in situ and ex situ techniques. Open/closed circles and diamonds correspond to short/long annealings, see main text for details.

shift of the T_{2g} mode to higher wavenumbers is readily visible. As the FWHM of the T_{2g} band varies less than 5% over the course of the transition, see Figure S6e (Supporting Information), its influence on the determination of the peak position can be neglected. It is noteworthy that the employed fast heating ramp of 100 °C min^{-1} did not impact the integrity of the CGO thin films, as shown by SEM imaging after a thermal cycle, see Figure S7 (Supporting Information). Possible laser related effects on oxygen exchange activity (i.e., direct laser heating or photoenhanced activity) were discarded by back-exchanging two samples simultaneously, with only one exposed to irradiation, as described in Figure S8 (Supporting Information). The resulting Raman shift at room temperature is the same for both samples, as shown in Figure S8b (Supporting Information) and therefore illumination effects can be safely neglected under chosen measurement conditions.

On the other hand, Pt is well known as a catalyst for oxygen reactions[50,51] and the employed Pt buffer layer could—upon diffusion to the surface—lead to modifications of the observed oxygen kinetics of ceria.[52,53] However, no such effect was found during exchange and back-exchange experiments by comparing CGO thin films simultaneously deposited on Pt/Si and MgO single-crystal substrates, as shown in Figure S9 (Supporting Information).

The gradual hardening of the normalized T_{2g} mode is shown in Figure 3b for different temperatures. Normalization is performed with respect to the theoretical mode position before any back-exchange, $\omega(t = 0)$. A clear thermal activation of the exchange process is observed. The (ω_{max}–T) diagram in Figure 3c shows the transitions from the initial ^{18}O to the final ^{16}O state, whereas the expected temperature evolution of $\omega(t = 0)$ and $\omega(t = \infty)$ is indicated with dashed lines. At high temperatures ($T \geqslant$ 450 °C), the initial part of the transients cannot be resolved, as the time scale of the isotopic exchange is comparable to the acquisition time.

The experimental data is modeled using Equation (6a,b) with a single and two parallel exponentials, respectively, as well as Equation (7) derived for non-linear reaction rates, as shown for the back-exchange transient at 400 °C in Figure 3b with a dotted (τ_{single}), dashed ($\tau_{parallel}$), and green dashed-dotted ($\tau_{non\text{-}lin.}$) line, respectively. The simplest case of a single exponential deviates considerably from the in situ data, whereas the other two models adequately fit the experimental transients. The deviations of the different models from the experimental data are shown in Figure S6 (Supporting Information). Two parallel saturation times are commonly related to different surface areas, such as grain boundary and lattice surface. It is noteworthy to mention that the grain size in the studied CGO thin films is much smaller than the size of the probing laser spot (1 μm^2), which means that different incorporation paths, e.g., within the grains and along the grain boundaries, will not be distinguished. The surface exchange coefficients of the $\tau_{parallel}$ model are shown in Figure 3d (open triangles). Both, k^*_α and k^*_β, follow an Arrhenius type behavior with an activation energy, E_A, of 0.9 ± 0.1 eV. This E_A is comparable to values reported in literature for Gd-doped CeO_2 within the analyzed temperature range.[54,55] Due to fast kinetics at 500 °C, only a single surface exchange coefficient could be estimated, which approximately falls onto the extrapolated Arrhenius law of k^*_α.

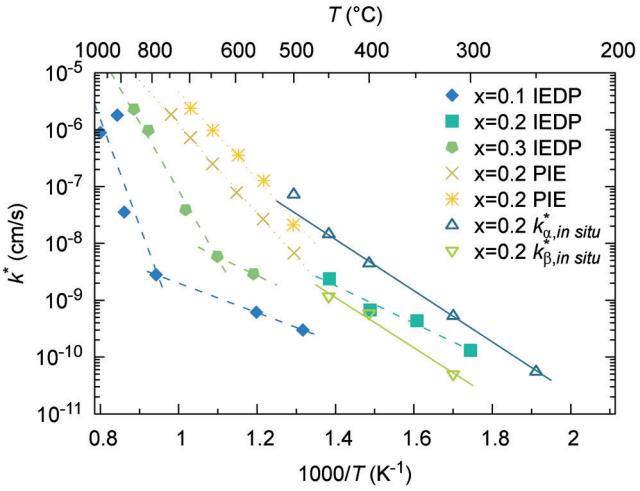

Figure 4. CGO surface exchange kinetics. Tracer surface exchange coefficients as reported in the literature for different types of $Ce_{1-x}Gd_xO_2$ samples obtained by IEDP or PIE, compared to in situ values found in this work: polycrystalline ceramics (x = 0.1 and x = 0.2 IEDP[55,56]), single-crystal CGO (x = 0.3 IEDP[57]), and CGO particles (x = 0.2 PIE[54,58]).

For samples not fully back-exchanged (i.e., $^{18}C > 10\%$), it is possible to estimate a k^* value based on ex situ measurements of the ^{18}C after the thermal annealing by analysing the room temperature Raman shift and measuring the ^{18}C by ToF-SIMS. This conventional approach can estimate only a single time constant, which is shown as well in Figure 3d. Interestingly, these values fall onto the lines of k^*_α and k^*_β depending on their annealing time. For short annealing durations of less than one hour, fast k^* values are found (open diamonds and open circles), while for an annealing of 20 h at 400 °C a slow k^* value is obtained (closed symbols, compare as well with SIMS depth profiles in Figure 2a). A similar effect was observed for the initial ^{18}O exchange in CGO. We can therefore conclude that simple linear kinetics indeed fail to model the observed processes and the time resolution of in situ IERS provides a richer insight into the physico-chemical processes than conventional approaches.

Figure 4 summarises surface exchange coefficients from this study and from the literature on different Gd-doped ceria samples, ranging from 10 to 31 mol%. Activation energies range from 2.5–4 eV at high temperatures, to around 1.5 eV at intermediate temperatures and down to 0.5–1 eV at low temperatures, while k^* varies between two to three orders of magnitude for different sample types and analysis techniques, including IEDP and pulsed isotope exchange (PIE). Note that the literature results presented are all obtained for ^{18}O exchange experiments, while in this study, we have studied in situ isotope back-exchanges to minimize the consumption of expensive ^{18}O tracer gas. However, tracer exchange and diffusion experiments are expected to be equivalent in both directions[59] and given a suitable temperature cell, IERS can readily be applied as well for the in situ analysis of the ^{18}O exchange.

Potential interactions with water vapor,[60] pO_2 dependence of k^*,[61] and the presence of catalytically active contaminations[54] have been discussed previously in the literature, but could not entangle the observed scatter of surface exchange coefficients, which is commonly found for many different fluorite and

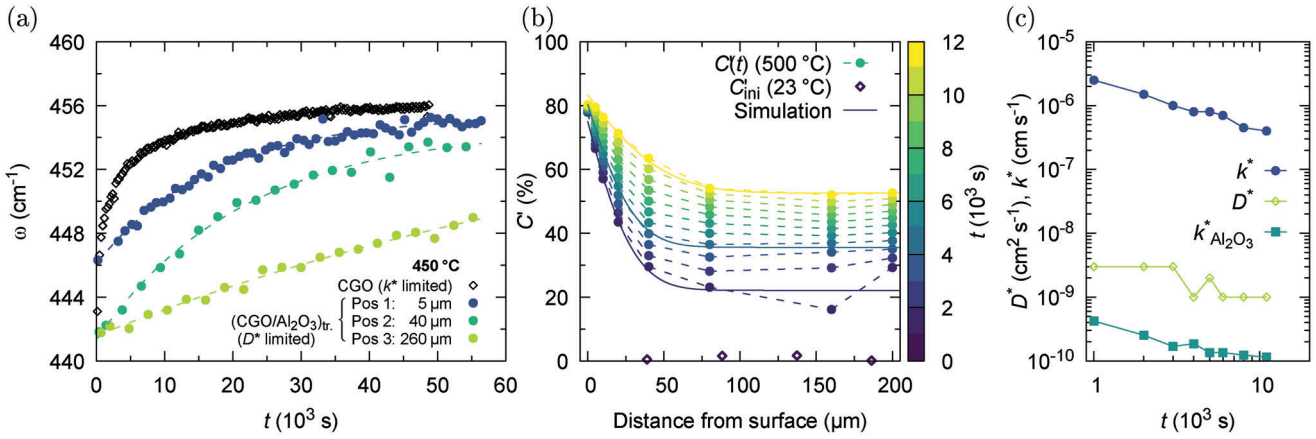

Figure 5. IERS for diffusion limited transport process. In-plane diffusion measurements on thin film CGO sample with a 40 nm Al_2O_3 capping layer. a) In situ Raman mode shift measured at 450 °C of CGO/Al_2O_3 with a trench (colored circles), measured at different in-plane distances from the open surface and uncoated CGO (open diamonds). b) Normalized isotopic fraction as a function of in-plane distance from open surface at 500 °C. Dashed lines connect interpolated data points at discrete times, t_i. Solid lines correspond to FEM simulations (COMSOL) for t_i = 1000, 4000, and 11 000 s, using three parameters (k^*, D^*, and $k^*_{Al_2O_3}$). c) Transport parameters as a function of time, obtained by FEM simulation of in situ data at 500 °C.

perovskite-type materials. It is interesting to note that k^* values obtained by Yoo via PIE connect well to our fast k^*_α values, where exchange times are very short (10 ms to 10 s), while the exchange experiments of Kowalski[55] with longer annealing times (4 h) compare well with the slower in situ time constants (i.e., k^*_β).

In a scenario of a partially blocking surface (e.g., inert particles on the surface of the CGO film), one of the two apparent in situ k^* values could correspond in reality to an in-plane diffusion process,[62] with diffusion coefficients in the range of 1×10^{-14} to 1×10^{-17} cm^2 s^{-1}. These values are orders of magnitude lower than D^* values obtained for CGO by in situ Raman spectroscopy or reported in the literature. Thus, it is implausible that one of the two parallel processes relates to a diffusion mechanism.

On the other hand, Rutman et al. found a dependence of k^* on the grain size of Gd-doped CeO_2 nano powder,[63] increasing by a factor of five from 5 to 50 nm. As shown in Figure S2b (Supporting Information), the samples studied here show a broad grain size distribution, which could cause the deviation from a single exponential behavior. This dependence could be potentially addressed by novel techniques based on isotope exchange coupled to atomic probe tomography with nanometric resolution,[64] which is beyond the scope of this study.

3.3. IERS for Diffusion Limited Transport Processes

The capability of IERS for the study of diffusion limited reactions in an unprecedented manner, is demonstrated using a CGO/Al_2O_3 model system, where oxygen exchange is enabled only at a trench along the centerline (see schematic in Figure S10, Supporting Information). Time resolved isotope diffusion profiles are obtained via consecutive line scans perpendicular to the trench, as shown in **Figure 5**a at 450 °C. At all x positions, a smooth transition can be observed, while the Raman mode shift becomes much slower with increasing distance to the open surface, due to the increasing diffusion length. In comparison to an un-capped CGO sample (open diamonds, surface limited process) kinetic differences are evident. In the next step, each transient was interpolated via curve fitting, as indicated with dashed lines, to obtain $\omega(x_i,t_i)$ at discrete times, t_i for all measured positions x_i, which can be converted into C' using the VCA approximation. The resulting isotopic diffusion profiles are shown in Figure 5b. Exchange and diffusion coefficients (k^* and D^*) were retrieved by comparing experimental data to FEM simulations (COMSOL, the used 2D geometry is shown in Figure S10, Supporting Information). Notably, C' is flat for $x > 80$ µm, but increases with time. In the simplest case this can be understood as a small leakage of oxygen through the alumina capping and can be considered by the introduction of an additional exchange coefficient, $k^*_{Al_2O_3}$, at the top surface. Representative least square solutions are shown for t_i =1000, 4000 and 11000 s with solid lines in Figure 5(b). Resulting diffusion coefficients ($D^* \approx 2 \times 10^{-9}$ cm s^{-2}) match well with literature values extrapolated to 500 °C ($D^*_{lit.} = 1 \times 10^{-9}$ to 1×10^{-8} cm s^{-2})[56,57] and $k^* \approx 4 \times 10^{-7}$ cm s^{-1} is in reasonable agreement with values reported above. The exchange through the capping layer is orders of magnitude slower, i.e. $k^*_{Al_2O_3} \approx 2 \times 10^{-10}$ cm s^{-1}.

Interestingly, diffusion profiles at different times cannot be fitted with the same set of transport parameters (k^*, $k^*_{Al_2O_3}$, and D^*), but must be optimized for each time. Evolution with time of the best matching values is shown in Figure 5c. Similar to the surface limited case described above, we find non-simple reaction kinetics that cannot be described with a single time constant for the surface exchange (side and top) and diffusion. This apparent time dependence of the surface exchange coefficients may be lifted by the introduction of different surface areas (as for the surface limited case, i.e., two parallel contributions), or the consideration of non-linear thermodynamics already for the simple case of a purely entropic driving force in tracer exchange experiments. Possessing the capability to address this type of questions renders one of the main advantages of IERS.

Finally, in situ measurements are validated by room temperature Raman mapping of the surface after the back-exchange, as shown in Figure S11a (Supporting Information). The isotopic in-plane gradient is readily visible via the wavenumber shift. The average line profile (solid line in the upper panel in Figure S11a, Supporting Information) is used to obtain transport properties via FEM simulations. The obtained values ($k^* = 4 \times 10^{-7}$ cm s^{-1}, $k^*_{Al_2O_3} = 7 \times 10^{-11}$ cm s^{-1} , and $D^* = 2 \times 10^{-9}$ cm s^{-2}) are in perfect agreement with the figures from in situ measurements, obtained for the last diffusion profile (t_i = 11 000 s). This validates that isotopic exchange Raman spectroscopy is a powerful tool for the characterization of mass-transport properties of oxide materials under in situ conditions.

4. Conclusion

Novel isotope exchange Raman spectroscopy (IERS) allows to directly measure tracer surface exchange and self-diffusion coefficients in situ with time and spatial resolution, not accessible by means of conventional techniques. We have used IERS to measure transport properties and corresponding activation energies for Gd-doped CeO_2 thin films. The obtained values are in good agreement with classical ex situ approaches and previously reported values. However, thanks to the time resolution of IERS, we were able to gain additional information depth opening up questions on the validity of simple linear irreversible reaction kinetics, which can be further addressed using this new methodology.

The strengths of IERS are its simple setup, fast and easy data acquisition and analysis, economic benefits and resource efficiency, and therefore its wide applicability for the study of functional oxides for energy applications and beyond as a function of various process parameters under in situ and operando conditions.

5. Experimental Section

$Ce_{1-x}Gd_xO_2$ (x = 0.2) thin films were fabricated by large-area pulsed laser deposition (PVD Systems, PLD 5000) equipped with a 248 nm KrF excimer laser (Lambda Physics, COMPex PRO 205) under the following conditions: temperature 700 °C, oxygen pressure 7×10^{-3} mbar, target to substrate distance 90 mm, laser fluency ≈1.2 J cm^{-2}, 10 Hz repetition rate. The oxide thin films were deposited on top of 10×10 mm^2 Si (111) wafers, coated with a Pt (150 nm)/TiO_2 (40 nm)/SiO_2 (500 nm) multilayer (LETI, Grenoble, France). After deposition, samples were cut into several pieces using a water cooled diamond saw. Thin (40–90 nm), conformal Al_2O_3 capping layers were deposited by atomic layer deposition (ALD) at 180 °C on top of the ^{18}O filled CGO thin films. Trenches were opened across the Al_2O_3 coating and CGO layer at the center of the sample with a diamond tip, exposing the out-of-plane CGO surface to the atmosphere.

For the isotope exchange, samples were placed in a sealed quartz tube, evacuated and purged with Ar for three times, before ^{18}O enriched oxygen was introduced ($c(^{18}O)$ = 98%, p = 0.2 atm, CK Isotopes, UK). Samples were rapidly heated by rolling on a tubular furnace with an approximate ramp of 100 °C min^{-1} to 640 °C. After 0.5 h, the furnace was rolled off. Pre-equilibration steps in natural oxygen, as commonly performed for tracer diffusion experiments, were omitted, as a high ^{18}O isotopic fraction was desired. For CGO, the oxygen vacancy concentration within the studied temperature window was fixed by the amount of Gd doping.[65,66] A temperature difference between the initial exchange and the subsequent back-exchange, was therefore not expected to cause an additional chemical driving force.

The chemical and isotopic composition was obtained by SIMS analysis, which was performed using a ToF-SIMS V instrument (ION-TOF GmbH Germany) equipped with a Bi liquid metal ion gun (LMIG) for analysis and a caesium (Cs^+) gun for sputtering. Negative secondary ions were collected and data were obtained in burst mode operation (six pulses), applying Poisson correction. Charge effects were compensated by means of a 20 eV pulsed electron flood gun. Depth profiling was performed by alternating sputtering of a 300 × 300 μm^2 surface area with the Cs^+ ion beam (2 keV, 110 nA) and chemical analysis with the Bi^{3+} primary ion beam (25 keV, 0.25 pA, rastered surface area: 50 × 50 μm^2). Generally two SIMS profiles per sample were recorded to confirm its homogeneity.

Raman spectroscopy measurements were performed using a Jobin Yvon/Horiba Labram spectrometer equipped with a liquid nitrogen cooled CCD detector (Jobin Yvon-Horiba Spectrum One CCD3000V). The blue excitation wavelength (488 nm) of an Ar^+ laser was focused onto the surface with an approximate spot size of 1 μm^2. A 50× (long working distance) and a 100× objective were used for in situ studies and room temperature measurements, respectively. The maximum laser power on the sample surface did not exceed 0.7–0.8 mW. Spectra were calibrated at room temperature using a silicon reference sample with a theoretical position of 520.7 cm^{-1}. The background was subtracted for each spectrum using a third-order polynomial.

For in situ back-exchange measurements, a temperature cell (Linkam THMS 600 and Nextron MPS-CHH) was mounted onto the Raman stage. The cells were equipped with a ceramic heater (diameter of 1'' Linkam, 0.5'' Nextron) and a sapphire window for Raman measurements. For spatial resolution, the temperature cell was mounted onto a motorized linear stage. The temperature cell was preheated for several hours before loading a sample to thermally equilibrate the setup and avoid the loss of focus due to thermal expansion during the measurement. Fast heating ramps of up to 100 °C min^{-1} were used to minimise any isotopic exchange during the heating. Automatic Raman acquisition was typically started within 30–60 s after reaching the exchange temperature, with acquisition times of 120–240 s. Isotopic back-exchanges were performed under flowing dry air (<100 ml min^{-1}) of natural ^{18}O composition at atmospheric pressure.

Supporting Information

Supporting Information is available from the Wiley Online Library or from the author.

Acknowledgements

This work has received funding from the European Union's Horizon 2020 research and innovation program under grant agreement no. 824072 (Harvestore) and no. 101017709 (EPISTORE) and under the Marie Skłodowska-Curie grant agreements no. 840787 (Thin-CATALYzER) (for F.B) and no. 746648 (PerovSiC) (for D.P.), as well as from the Agence National de la

Recherche for project ANR-15-CE24-0018 (Alps Memories). The authors acknowledge Stefano Ambrosio for his help with initial IERS measurements, Nicolas Nuns for his assistance with SIMS measurements and Florence Robaut and Laetitia Rapenne for FIB lamella preparation and TEM analysis. This research has benefited from characterization equipment of the Grenoble INP - CMTC platform supported by the Centre of Excellence of Multifunctional Architectured Materials "CEMAM" n°ANR-10-LABX-44-01 funded by the "Investments for the Future" Program. In addition, this work has been performed with the help of the "Plateforme Technologique Amont" de Grenoble, with the financial support of the "Nanosciences aux limites de la Nanoélectronique" Fundation'' and CNRS Renatech network. Chevreul institute (FR 2638), the French ministry of research, the Région Hauts de France and FEDER are acknowledged for supporting and funding the surface analysis platform (ToF-SIMS).

Conflict of Interest

The authors declare no conflict of interest.

Author Contributions

Conceptualization: M.B., A.S.; sample preparation: F.B., F.C., A.S.; investigation: A.S., C.P., M.M.; formal analysis: A.S.; methodology: A.S., M.B., O.C., D.P., C.J., M.M.; original draft: A.S.; review & editing: all authors.

Data Availability Statement

The data that support the findings of this study are openly available in Zenodo at https://doi.org/10.5281/zenodo.7072918, reference number 7072918.

Keywords

energy applications, functional oxides, in situ methodology, oxygen isotope exchange, Raman spectroscopy, surface kinetics, tracer diffusion

Received: April 7, 2023
Revised: May 17, 2023
Published online: July 2, 2023

[1] C. Sun, J. A. Alonso, J. Bian, *Adv. Energy Mater.* **2021**, *11*, 2000459.
[2] M. Acosta, F. Baiutti, A. Tarancón, J. L. MacManus-Driscoll, *Adv. Mater. Interfaces* **2019**, *6*, 1900462.
[3] A. Stangl, A. Riaz, L. Rapenne, J. M. Caicedo, J. d. D. Sirvent, F. Baiutti, C. Jiménez, A. Tarancón, M. Mermoux, M. Burriel, *J. Mater. Chem. A* **2022**, *10*, 2528.
[4] S. Hwang, X. Chen, G. Zhou, D. Su, *Adv. Energy Mater.* **2020**, *10*, 1902105.
[5] A. K. Opitz, A. Nenning, C. Rameshan, M. Kubicek, T. Götsch, R. Blume, M. Hävecker, A. Knop-Gericke, G. Rupprechter, B. Klötzer, J. Fleig, *ACS Appl. Mater. Interfaces* **2017**, *9*, 35847.
[6] X. Li, H.-Y. Wang, H. Yang, W. Cai, S. Liu, B. Liu, *Small Methods* **2018**, *2*, 1700395.
[7] A. Stangl, D. Muñoz-Rojas, M. Burriel, *J. Phys. Energy* **2021**, *3*, 012001.
[8] Q. Meyer, Y. Zeng, C. Zhao, *Adv. Mater.* **2019**, *31*, 1901900.
[9] S. T. Oyama, W. Li, *Top. Catal.* **1999**, *8*, 75.
[10] S. Kuba, H. Knözinger, *J. Raman Spectrosc.* **2002**, *33*, 325.
[11] G. Mestl, M. A. Bañares, in *In-Situ Characterization of Heterogeneous Catalysts*, vol. *158*, John Wiley & Sons, Ltd, New York **2013**, pp. 267–292.
[12] H. Kanoh, W. Tang, K. Ooi, *Electrochem. Solid-State Lett.* **1998**, *1*, 17.
[13] W. Huang, R. Frech, *J. Power Sources* **1999**, *81-82*, 616.
[14] S. Migge, G. Sandmann, D. Rahner, H. Dietz, W. Plieth, *J. Solid State Electrochem.* **2005**, *9*, 132.
[15] V. Stancovski, S. Badilescu, *J. Appl. Electrochem.* **2014**, *44*, 23.
[16] B. K. Kim, H. O. Hamaguchi, *Phys. Status Solidi B* **1997**, *203*, 557.
[17] M. Guerain, M. Mermoux, C. Duriez, *Corros. Sci.* **2015**, *98*, 140.
[18] C. Ciszak, M. Mermoux, G. Gutierrez, F. Leprêtre, C. Duriez, I. Popa, L. Fayette, S. Chevalier, *J. Raman Spectrosc.* **2019**, *50*, 425.
[19] B.-K. Kim, S. J. Park, H.-o. Hamaguchi, *J. Am. Ceram. Soc.* **1994**, *77*, 2648.
[20] D. Stender, S. Heiroth, T. Lippert, A. Wokaun, *Solid State Ionics* **2013**, *253*, 185.
[21] G. Mestl, P. Ruiz, B. Delmon, H. Knözinger, *Russ. J. Phys. Chem.* **1994**, *98*, 11283.
[22] G. Mestl, P. Ruiz, B. Delmon, H. Knözinger, *Russ. J. Phys. Chem.* **1994**, *98*, 11269.
[23] G. Tsilomelekis, S. Boghosian, *Catal. Today* **2010**, *158*, 146.
[24] E. L. Lee, I. E. Wachs, *The Russ. J. Phys. Chem. C* **2008**, *112*, 6487.
[25] B. M. Weckhuysen, J. M. Jehng, I. E. Wachs, *Russ. J. Phys. Chem. B* **2000**, *104*, 7382.
[26] B.-K. Kim, S.-J. Park, H.-o. Hamaguchi, *J. Am. Ceram. Soc.* **1993**, *76*, 2119.
[27] A. Moreira Da Silva, T. Steiner, W. Saenger, J. Empis, J. J. Teixeira-Dias, *Chem. Commun.* **1996**, 1871, https://pubs.rsc.org/en/content/articlelanding/1996/CC/CC9960001871.
[28] J. Gao, Y. Meng, A. Benton, J. He, L. G. Jacobsohn, J. Tong, K. S. Brinkman, *ACS Appl. Mater. Interfaces* **2020**, *12*, 38012.
[29] J. Gao, Y. Meng, J. H. Duffy, K. S. Brinkman, *Adv. Energy Sustainability Res.* **2021**, *2*, 2100098.
[30] A. Schmid, M. Krammer, J. Fleig, *Adv. Energy Mater.* **2023**, *13*, 2203789.
[31] M. Cardona, M. L. Thewalt, *Rev. Mod. Phys.* **2005**, *77*, 1173.
[32] M. Mermoux, C. Duriez, *J. Raman Spectrosc.* **2021**, *52*, 2131.
[33] The opened side surface must be sufficiently large to avoid any out-of-plane isotopic gradient, especially relevant for bulk materials with anisotropic diffusion properties. Alternatively to cutting a trench, one side surface can be left uncapped in bulk samples.
[34] A. Karthikeyan, S. Ramanathan, *Appl. Phys. Lett.* **2008**, *92*, 2006.
[35] R. Moreno, P. García, J. Zapata, J. Roqueta, J. Chaigneau, J. Santiso, *Chem. Mater.* **2013**, *25*, 3640.
[36] M. Katsuki, S. Wang, K. Yasumoto, M. Dokiya, *Solid State Ionics* **2002**, *154-155*, 589.
[37] F. Noll, W. Münch, I. Denk, J. Maier, *Solid State Ionics* **1996**, *86-88*, 711.
[38] J. Maier, *Physical Chemistry of Ionic Materials*, vol. *12*, John Wiley & Sons, Ltd, Chichester, UK **2004**.
[39] The net flux vanishes at equilibrium, thus k_0^* must be 0.
[40] L. Chen, C. L. Chen, A. J. Jacobson, *IEEE Trans. Appl. Supercond.* **2003**, *13*, 2882.
[41] G. Kim, S. Wang, A. J. Jacobson, C. L. Chen, *Solid State Ionics* **2006**, *177*, 1461.
[42] L. Yan, B. Kavaipatti, K.-C. Chang, H. You, P. Salvador, *ECS Trans.* **2019**, *35*, 2063.
[43] M. Formenti, H. Courbon, F. Juillet, A. Lissatchenko, J. R. Martin, P. Meriaudeau, S. J. Teichner, *J. Vac. Sci. Technol.* **1972**, *9*, 947.
[44] P. Pichat, H. Courbon, R. Enriquez, T. T. Y. Tan, R. Amal, *Res. Chem. Intermed.* **2007**, *33*, 239.
[45] R. Merkle, R. A. De Souza, J. Maier, *Angew. Chem., Int. Ed.* **2001**, *40*, 2126.
[46] R. Merkle, J. Maier, *Phys. Chem. Chem. Phys.* **2002**, *4*, 4140.
[47] T. Defferriere, D. Klotz, J. C. Gonzalez-Rosillo, J. L. Rupp, H. L. Tuller, *Nat. Mater.* **2022**, *21*, 438.

[48] J. R. McBride, K. C. Hass, B. D. Poindexter, W. H. Weber, *J. Appl. Phys.* **1994**, *76*, 2435.
[49] N. Yang, Y. Shi, S. Schweiger, E. Strelcov, A. Belianinov, V. Foglietti, P. Orgiani, G. Balestrino, S. V. Kalinin, J. L. M. Rupp, C. Aruta, *ACS Appl. Mater. Interfaces* **2016**, *8*, 14613.
[50] Y. Ma, T. E. Burye, J. D. Nicholas, *J. Mater. Chem. A* **2021**, *9*, 24406.
[51] H. Uchida, M. Yoshida, M. Watanabe, *J. Electrochem. Soc.* **1999**, *146*, 1.
[52] A. Bruix, A. Migani, G. N. Vayssilov, K. M. Neyman, J. Libuda, F. Illas, *Phys. Chem. Chem. Phys.* **2011**, *13*, 11384.
[53] H. G. Seo, Y. Choi, W. Jung, *Adv. Energy Mater.* **2018**, *8*, 1703647.
[54] M. Schaube, R. Merkle, J. Maier, *J. Mater. Chem. A* **2019**, *7*, 21854.
[55] K. Kowalski, *Defect and Diffusion Forum* **2009**, *289-292*, 769.
[56] P. S. Manning, J. D. Sirman, J. A. Kilner, *Solid State Ionics* **1996**, *93*, 125.
[57] E. Ruiz-Trejo, J. D. Sirman, Y. M. Baikov, J. A. Kilner, *Solid State Ionics* **1998**, *113-115*, 565.
[58] C.-Y. Yoo, Ph.D. thesis, Universiteit Twente, Enschede, The Netherlands **2012**, https://research.utwente.nl/en/publications/phase-stability-and-oxygen-transport-properties-of-mixed-ionic-el.
[59] S. J. Cooper, M. Niania, F. Hoffmann, J. A. Kilner, *Phys. Chem. Chem. Phys.* **2017**, *19*, 12199.
[60] S. P. Waldow, B. J. Statham, H. F. Wardenga, T. E. Weirich, A. Klein, R. A. De Souza, *ACS Appl. Mater. Interfaces* **2020**, *12*, 36768.
[61] J. A. Lane, J. A. Kilner, *Solid State Ionics* **2000**, *136-137*, 927.
[62] W. Preis, *J. Solid State Electrochem.* **2019**, *23*, 1089.
[63] J. Rutman, M. Kilo, S. Weber, I. Riess, *Solid State Ionics* **2014**, *265*, 29.
[64] F. Baiutti, F. Chiabrera, D. Diercks, A. Cavallaro, L. Yedra, L. López-Conesa, S. Estradé, F. Peiró, A. Morata, A. Aguadero, A. Tarancón, *Adv. Mater.* **2021**, *33*, 2105622.
[65] K. Yashiro, S. Onuma, A. Kaimai, Y. Nigara, T. Kawada, J. Mizusaki, K. Kawamura, T. Horita, H. Yokokawa, *Solid State Ionics* **2002**, *152-153*, 469.
[66] S. Wang, H. Inaba, H. Tagawa, M. Dokiya, T. Hashimoto, *Solid State Ionics* **1998**, *107*, 73.